Antiferromagnetic resonance in EuTe

P. K. Streit* and Glen E. Everett
Physics Department, University of California, Riverside, California 92521
(Received 26 February 1979)

Previous measurements of the low-frequency branch of the "easy-plane" antiferromagnet have been extended to the high-frequency branch. The resonance fields as a function of angle at constant frequencies greater and less than the zero-field resonance frequency, ω_c, have been measured and analyzed based on resonance equations including the dipolar and a phenomenological uniaxial anisotropy energy. Good agreement is obtained for branches associated with the different T domains. Deviations, attributed to domain-wall effects, are observed. The zero-field resonance frequency, ω_c, has been determined from measurements of ω vs H with $\vec{H}$ in an easy plane. The decrease in $\omega_c(T)$ with increasing temperature is proportional to $T^{3/2}$ and is the same as found for the critical (exchange) field by Oliveira *et al.* The frequency ω_c at $T=0$ corrected for demagnetizing effects corresponds to a dipolar interaction, $K_d=0.817\times10^6$ erg/cm^3, which is ~10% larger than the classically calculated value for EuTe. The exchange field, H_E, determined from the variation ω vs H with $\vec{H}$ in an easy plane was obtained. The value at $T=0$ and corrected for demagnetizing effects is $H_E(0)=73.0$ kOe compared with the value $H_E=72.2$ kOe determined directly by Oliveira *et al.* This excellent agreement is considered fortuitous.

I. INTRODUCTION

The magnetic semiconductor EuTe is fcc (NaCl) in the paramagnetic phase and orders in the type-II antiferromagnetic configuration at $T_N=9.8$ K. The magnetic order is represented by ferromagnetic spin alignment within (111) planes and the moments of adjacent plans being antiparallel. From an investigation of the angular dependence of the antiferromagnetic resonance (AFMR[1]) it has been shown that EuTe is an "easy-plane" (EP) antiferromagnet (AFM) with the moments lying in the (111) planes. The ⟨111⟩ directions with which magnetic order is associated are the body diagonals of the paramagnetic phase. The fourfold degeneracy in the paramagnetic phase results in the formation of T domains in a real sample when cooled below T_N. The multiple-resonance branches observed[1] are associated with different macroscopic T-domain regions in a finite sample.

Turov[2] has analyzed the uniaxial AFM in terms of the mean-field ground-state Hamiltonian

$$\frac{H_0}{V}=\tfrac{1}{2}A\,\vec{m}^{\,2}+\tfrac{1}{2}am_z^2+\tfrac{1}{2}bl_z^2-\vec{m}\cdot\vec{h}\ , \tag{1}$$

where z is the principle symmetry axis direction. The magnetic $\vec{m}$ and antiferromagnetic $\vec{l}$ vectors[3] are defined in terms of the sublattice moments $\vec{M}_1$ and $\vec{M}_2$ by

$$\vec{m}=\frac{\vec{M}_1+\vec{M}_2}{M_0},\quad \vec{l}=\frac{\vec{M}_1-\vec{M}_2}{M_0}\ , \tag{2}$$

where $M_1^2=M_2^2=(\frac{1}{2}M_0)^2$. The first and fourth terms represent the exchange and Zeeman energies respectively while the second and third are associated with magnetocrystalline anisotropy. The condition $b>0$ gives rise to EP behavior with $\vec{l}$ lying in the plane perpendicular to z. The resonance equations consist of two branches; $\vec{H}\parallel\vec{z}$:

$$\frac{\omega^+}{\gamma}=(H_{EA}^2+H^2)^{1/2}\ , \tag{3a}$$

$$\frac{\omega^-}{\gamma}=0\ , \tag{3b}$$

and $\vec{H}\perp\vec{z}$:

$$\frac{\omega^+}{\gamma}=H_{EA}(1-H^2/H_E^2)^{1/2}\ , \tag{4a}$$

$$\frac{\omega^-}{\gamma}=H(1+a/A)^{1/2}\ , \tag{4b}$$

where H_E and H_{AE} are the exchange and exchange-anisotropy fields, respectively.[4] Introducing the dimensionless quantities

$$x=\frac{\omega}{\gamma H_E},\quad h=\frac{H}{H_E},\quad X_c=\frac{H_{EA}}{H_E}\ ,$$

the dependence of the resonance frequencies on field are shown in Figs. 1(a) and 1(b) for Eqs. (3) and (4), respectively. The low-frequency branch ω^-, Eq. (4b), for $\vec{H}$ in or near an EP was observed in Ref. 1.

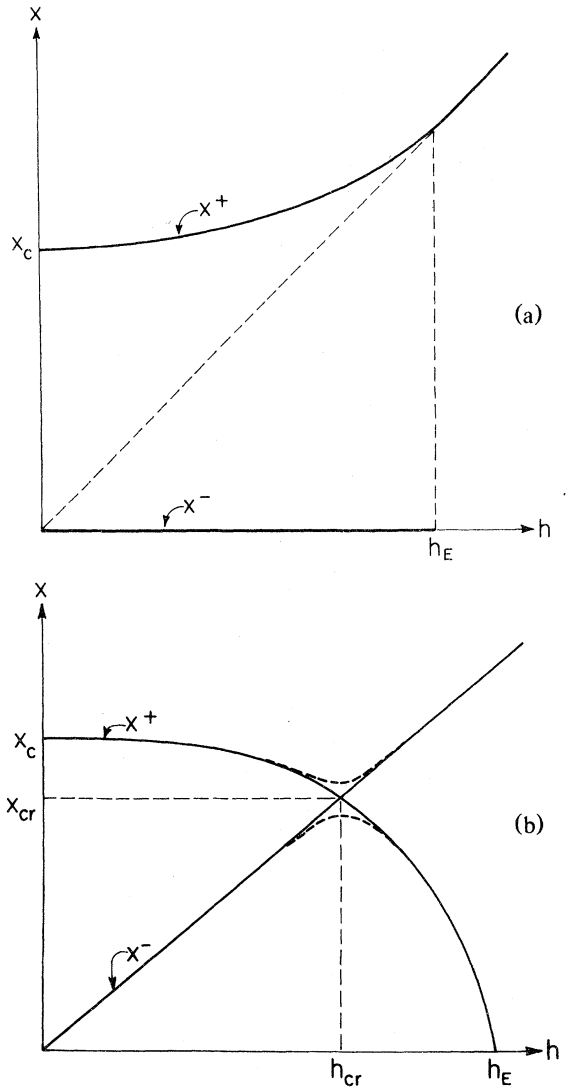

FIG. 1. (a) Resonance frequencies X^+ and X^- ($X=\omega/\gamma H_E$) vs field $h=H/H_E$ for $\vec{h}$ along the "hard" axis of an easy-plane AFM. The 45° dashed line represents the asymptotic limiting behavior in the paramagnetic phase $h>h_E$. The lower branch $X^-=0$ results when anisotropy in the EP is neglected. (b) Same as 1(a), but with $\vec{h}$ in the easy plane. The linear dependence of X^- on h is a consequence of neglecting anisotropy in the easy plane. When easy-plane anisotropy is included, $X^-\neq 0$ at $h=0$, Ref. 5. The dashed lines in the vicinity of the mode crossing at (h_{cr},X_{cr}) represent schematically the effect of mode coupling when higher-order anisotropy contributions are included.

Battles and Everett[5] determined the angular dependence of the low-frequency branch at 9, 18, and 24 GHz and 1.17 K. Expressions for the low-frequency–low-field angular dependence were determined based on the dipolar and phenomenological "in plane" anisotropy energies. Analysis of the data gave the values

$$H_a=8\pm 4 \text{ Oe and } H_A=4.0\pm 0.4 \text{ kOe}$$

for the in-plane and dipolar anisotropy fields, respectively. The calculated zero-field critical frequencies were

$$\omega_c^-=2 \text{ GHz}, \quad \omega_c^+=68 \text{ GHz} .$$

The dipolar anisotropy field determined is ~20% lower than Kaplan's[6] value calculated classically. Nakai *et al.*[7] have measured the AFMR in EuTe at 9.2 and 33.99 GHz. Their results are in good qualitative agreement with those of Ref. 5. The value of the dipolar anisotropy term determined from data at 1.7 K is $\sim\frac{2}{3}$ of Kaplan's value for $T=0$. Masset and Callaway[8] have used the values ω_c^- and ω_c^+ as energy gaps in a spin-wave calculation of the zero-field specific heat obtaining good agreement with Passenheim's results.[9]

The present authors have investigated the high-frequency branch of the AFMR in the frequency interval 60–90 GHz. A report of initial results is given in Ref. 10. The angular dependence of the resonance field for $\omega>\omega_c$ was determined and is in good qualitative agreement with theory. Measurements of resonant frequency versus H for H along the hard axis and in the easy plane were used to determine the zero-field frequency ω_c and exchange field H_E at different temperatures. The frequency ω_c was found to decrease as $T^{3/2}$ for $T/T_N<\frac{1}{3}$ and more rapidly as T_N is approached. In the present paper we present more detailed measurements of the angular and temperature dependence of the AFMR at frequencies above and below ω_c. Anticipating our experimental results, the frequency ω_c extrapolated to $T=0$ corresponds to a dipolar interaction ~10% *greater* than the classically calculated value.[6] In Sec. II the resonance equations and their angular dependence are described followed by a description of experimental details in Sec. III. The experimental results are described in Sec. IV and discussed in Sec. V.

II. RESONANCE EQUATIONS

The free energy, F, is represented by

$$F=F_{ex}+F_z+F_A \ , \tag{5}$$

where the terms correspond to the exchange, Zeeman, and anisotropy energies, respectively. The anisotropy energy, F_A, is represented by

$$F_A=F_{dd}+F_{ua}+F_{bp} \tag{6}$$

corresponding to dipolar, uniaxial, and in-plane (basal-plane) contributions. The sublattice magnetization vectors $\vec{M}_1$ and $\vec{M}_2$ are transformed into the

dimensionless set $\vec{m}$ and $\vec{l}$ and the applied field $\vec{H}$ by

$$\vec{m}=\frac{\vec{M}_1+\vec{M}_2}{2M_0},\quad \vec{l}=\frac{\vec{M}_1-\vec{M}_2}{2M_0},\quad \vec{h}=\frac{\vec{H}}{2M_0}\ ,$$

where M_0 represents[11] the sublattice moment at $T=0$. The vectors $\vec{m}$ and $\vec{l}$ are coupled by the relations

$$\vec{m}^2+\vec{l}^2=1,\quad \vec{m}\cdot\vec{l}=0\ . \tag{7}$$

Battles and Everett[5] have shown that F_{bp} is small causing $\langle 11\bar{2}\rangle$ easy directions in a (111) plane. The estimated spin-flop field in EuTe is $H_F\sim 700$ Oe. Restricting the calculation to fields $H >> H_F$, F_{bp} can be neglected, and the dimensionless free energy, F', can be expressed

$$F'=(\lambda_2+\kappa_d)\,\vec{m}^2+\kappa_a m_z^2+(3\kappa_d+\kappa_a)\,l_z^2-2\,\vec{m}\cdot\vec{h}\ , \tag{8}$$

where the various terms are: λ_2, antiferromagnetic exchange (J_2 in EuTe); κ_d, dipolar; and κ_a, uniaxial energies. The z axis corresponds to a $\langle 111\rangle$ direction in EuTe. The static properties of the system are obtained by minimizing F' with respect to $\vec{m}$ and $\vec{l}$ subject to the constraints, Eq. (7). Representing the static field by

$$\vec{h}_0=(h_{0x},0,h_{0z})\ ,$$

the solutions are

$$m_{0x}=\frac{h_{0x}}{\lambda_2+\kappa_d},\quad m_{0y}=0,\quad m_{0z}=\frac{h_{0z}}{\lambda_2+\kappa_d+\kappa_a} \tag{9}$$

and

$$l_{0x}=0,$$

$$l_{0y}=\left[1-\left(\frac{h_{0x}}{\lambda_2+\kappa_d}\right)^2-\left(\frac{h_{0z}}{\lambda_2+\kappa_d+\kappa_a}\right)^2\right]^{1/2},$$

$$l_{0z}=0 \tag{10}$$

subject to the condition $h<h_E$ where h_E is the exchange field.[12] For $h>h_E$, $\vec{m}^2=1$ and $\vec{l}=0$. Representing the angles of $\vec{m}$ and $\vec{h}$ with respect to the z axis as α and β, respectively, one obtains

$$\sin(\beta-\alpha)=\frac{\kappa_a}{2h}\sin 2\alpha,\quad h>h_E(\beta)\ . \tag{11}$$

The asymptotic approach to colinearity of $\vec{m}$ and $\vec{h}$ at high fields is the same for a uniaxial ferromagnet above technical saturation. Having neglected the in-plane anisotropy energy, F_{bp}, gives the result

$$\vec{l}\cdot\vec{h}=0$$

at all fields and corresponds to the "spin-flopped" state.

The equations of motion for $\vec{m}$ and $\vec{l}$ are

$$\frac{1}{2M_0\gamma}\frac{d\vec{m}}{dt}=\vec{m}\times\frac{\partial F'}{\partial\vec{m}}+\vec{l}\times\frac{\partial F'}{\partial\vec{l}} \tag{12a}$$

and

$$\frac{1}{2M_0\gamma}\frac{d\vec{l}}{dt}=\vec{m}\times\frac{\partial F'}{\partial\vec{l}}+\vec{l}\times\frac{\partial F'}{\partial\vec{m}}\ . \tag{12b}$$

For small oscillating magnetic fields, $\vec{h}_1$, the time dependence

$$\vec{h}=\vec{h}_0+\vec{h}_1e^{i\omega t}\ ,$$

$$\vec{m}=\vec{m}_0+\vec{m}_1e^{i\omega t},\quad \vec{l}=\vec{l}_0+\vec{l}_1e^{i\omega t}\ ,$$

is substituted into Eqs. (12a) and (12b) and the equations solved in the small-signal harmonic approximation. The results can be expressed in the form

$$\vec{m}_1=\chi(m)\,\vec{h}_1,\quad \vec{l}_1=\chi(l)\,\vec{h}_1\ . \tag{13}$$

The resonance frequencies are determined by setting the determinant of the coefficients, Δ, equal to zero. Defining the dimensionless frequency $X=\omega/2M_0\gamma$ gives

$$\Delta=-X^2(X^2-X^{+2})(X^2-X^{-2})\ , \tag{14}$$

where the resonance frequencies X^+ and X^- are given by

$$(X^{\pm})^2=\tfrac{1}{2}\Big[X_c^2l_{0y}^2+h_{0x}(h_{0x}+\kappa_a m_{0z})+(h_{0z}-\kappa_a m_{0z})^2$$
$$\pm\{[X_c^2l_{0y}^2+h_{0x}(h_{0x}+\kappa_a m_{0x})+(h_{0z}-\kappa_a m_{0z})^2]^2-4h_{0x}(h_{0x}+\kappa_a m_{0x})X_c^2l_{0y}^2\}^{1/2}\Big]\ . \tag{15}$$

The frequency

$$X_c^2=(\lambda_2+\kappa_d)(3\kappa_d+\kappa_a) \tag{16}$$

corresponds to the zero-field resonance frequency, Figs. 1(a) and 1(b).

The relations between $\vec{m}_1$ and $\vec{l}_1$ and the oscillating magnetic field $\vec{h}_1$ have been presented, Eq. (13), in the form of susceptibility tensors. The elements of these terms are given in the Appendix. We note that the fields conjugate to $\vec{m}$ and $\vec{l}$ are $\vec{h}$ and $\vec{h}_{st}$, where $\vec{h}_{st}$ is the staggered magnetic field and is experimentally inaccessible. ($\vec{h}_{st}=0$ in the spin-flopped state.) The generalized susceptibility tensor would be written

$$\begin{pmatrix}\vec{m}\\ \vec{l}\end{pmatrix}=\begin{pmatrix}\vec{\chi}(mm), & \vec{\chi}(ml)\\ \vec{\chi}(lm), & \vec{\chi}(ll)\end{pmatrix}\begin{pmatrix}\vec{h}\\ \vec{h}_{st}\end{pmatrix}\ , \tag{17}$$

where

$$\vec{\chi}(m) \equiv \vec{\chi}(mm), \quad \vec{\chi}(\vec{1}) \equiv \vec{\chi}(lm) \ .$$

The general symmetry relation

$$\chi_{ik}(-\omega) = \chi_{ki}^{*}(\omega)$$

is satisfied by $\vec{\chi}(m)$ but not by the off-diagonal submatrix $\vec{\chi}(l)$ as defined by Eq. (13). In the general case power dissipation is determined by the relation

$$\frac{dQ}{dt} = \tfrac{1}{4} i\omega \sum_{j,k} (\chi_{jk}^{*} - \chi_{kj}) h_{lj} h_{lk}^{*} \tag{18}$$

rather than just the imaginary part of the susceptibility tensor, e.g., $\vec{\chi}(m)$ or $\vec{\chi}(l)$.

The resonance frequency dependence on field for $\vec{h}$ parallel and perpendicular to the EP is given in the Appendix, Eqs. (A3a), (A3b), (A4a), and (A4b). The functional dependence on the field is the same as obtained by Turov[2] but expressed in terms of the dipolar, κ_d, and uniaxial, κ_a, anisotropy energy contributions. The variation with field for these directions is shown in Figs. 1(a) and 1(b). The behavior of X^- at low fields is not exact owing to our neglect of the in-plane anisotropy energy[5] in this calculation. The low-frequency branch, X^-, for h in the easy plane is characterized by susceptibility components $\chi_{ij}(m)$ proportional to the induced magnetization m_{0x} $(i,j = y,z)$. Their smallness as $\vec{h} \to 0$ would explain, in part, the difficulty associated with the observation of this branch in the related materials, MnO and NiO. The branches X^+ and X^- cross at the field, h_{cr}, given by

$$h_{cr}^2 = \left(\frac{\lambda_2 + \kappa_a}{\lambda_2 + 4\kappa_d + 2\kappa_a} \right) X_c^2 \tag{19}$$

for $\vec{h}$ in the easy plane, Fig. 1(b). Mode coupling between X^+ and X^- branches due to the in-plane anisotropy energy and other higher-order terms is expected to modify the behavior near h_{cr} as represented by the dashed lines in Fig. 1(b).

A. Demagnetizing factor

The demagnetizing energy for an ellipsoidal sample is

$$F_n = \tfrac{1}{2} \vec{M} \cdot \vec{N} \cdot \vec{M} \ , \tag{20}$$

which reduces to

$$F_n = \tfrac{1}{2} \bar{N} \vec{M}^2, \quad \bar{N} = \frac{4\pi}{3} \ ,$$

for a sphere. The demagnetizing energy, added to Eq. (8) as the dimensionless quantity F_n', has the same functional dependence on $\vec{m}$ as the isotropic exchange, λ_2. The resonance frequencies and susceptibility tensor components are corrected for sample demagnetization in the case of a sphere by the replacement

$$\lambda_2 \to \lambda_2 + \tfrac{1}{2} \bar{N} \ ,$$

when $h < h_E$. The zero-field resonance frequency, X_c, Eq. (1b), is replaced by

$$X_c^2 = (\lambda_2 + \kappa_d + \tfrac{1}{2} \bar{N})(3\kappa_d + \kappa_a) \ . \tag{21}$$

The ratio of demagnetization to exchange energies is small but finite in EuTe. This correction is important in the determination of the dipolar anisotropy from experimental results. The importance of spherical samples is that the demagnetizing factor is determined and the effective demagnetizing field is spatially homogeneous within the sample. Nonspherical (ellipsoidal) samples having an inhomogeneous demagnetizing field will also have an inhomogeneous critical frequency X_c. The result would be an inhomogeneous line broadening in X^+ particularly in the low-field region.

B. Multidomain resonance behavior

Real macroscopic samples will be characterized by T domains corresponding to each of the $\langle 111 \rangle$ directions. The resonance behavior for an arbitrary field direction would be a superposition of two resonances from each of the four possible domains. The complicated composite dependence on field and angle has been observed. The general expression for the resonance frequencies, Eq. (15), has been studied numerically with the resonance frequencies for each of the four possible domains being determined at each angle of the applied field. Figures 2–4 show the resonance fields for individual and/or degenerate T domains as a function of field direction in the (100), (110), and (111) planes, respectively. The curves shown were computed with $\kappa_a = 0$ and illustrate the symmetry of resonances in the different planes. Each curve, labeled n, n', or n'' corresponds to the angular dependence of the resonance field, H_R, at a fixed frequency for a different domain. For $X = X_c$ ($\omega_5 = \omega_c$ in the figures), solutions with $H \neq 0$ exist, curves "5". The solution $H = 0$ is also allowed. A second critical frequency,

$$\omega_2 = \frac{\omega_c}{[1 + (3\kappa_a + \kappa_a)/(\lambda_2 + \kappa_a + \kappa_a)]^{1/2}} \ ,$$

exists which can be observed at a *single* angle for a given T domain and labeled as "2" (a single point) in the figures. It corresponds to the mode crossing frequency, X_{cr}, for $\vec{h}$ in the easy plane, Fig. 1(b), of a particular domain.

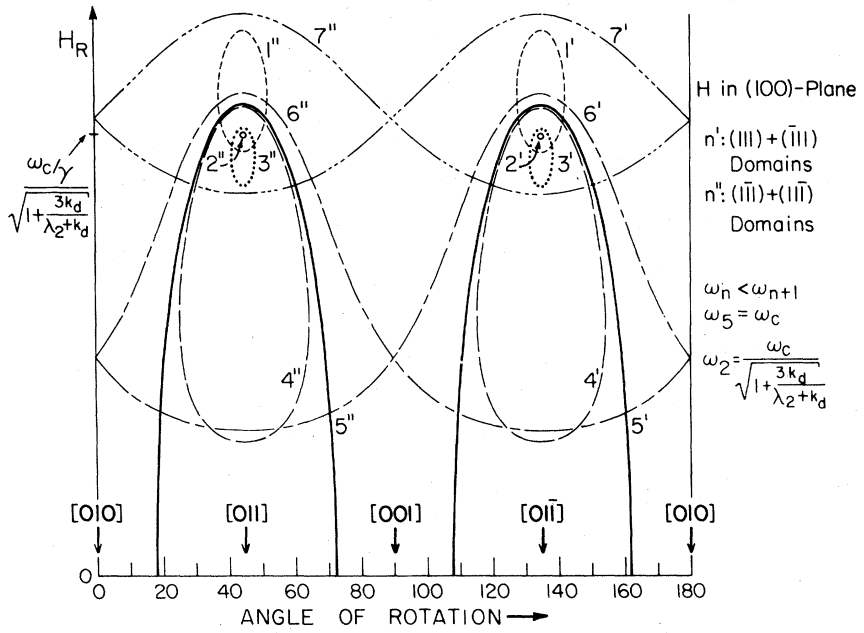

FIG. 2. Multidomain structure and anisotropy of the resonant field of an fcc type-II antiferromagnet with dipolar anisotropy, for the magnetic field lying in a (100) plane.

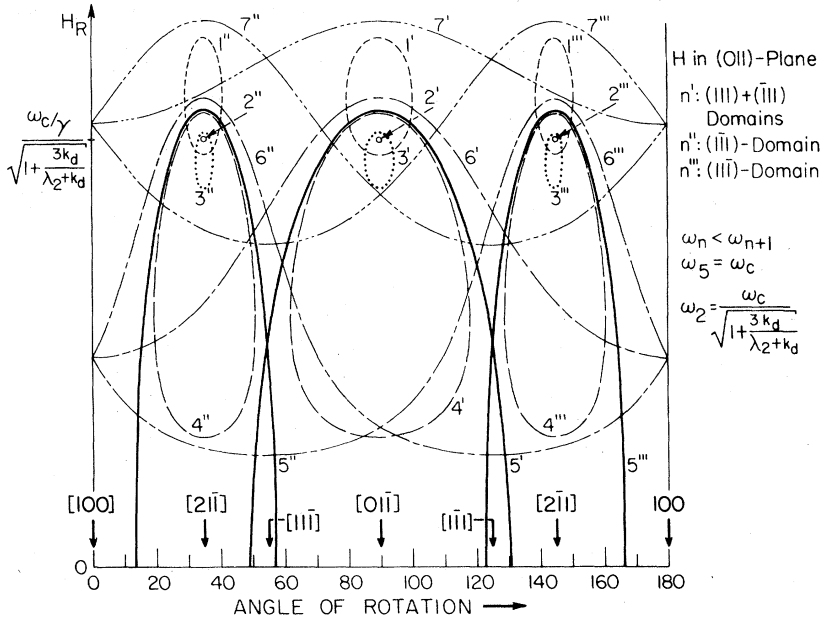

FIG. 3. Multidomain structure and anisotropy of the resonant field of an fcc type-II antiferromagnet with dipolar anisotropy, for the magnetic field lying in a (011) plane. [The curves labeled n' represent the angular dependence of the resonant field for the domain(s) characterized by a prime at the frequency ω_n.]

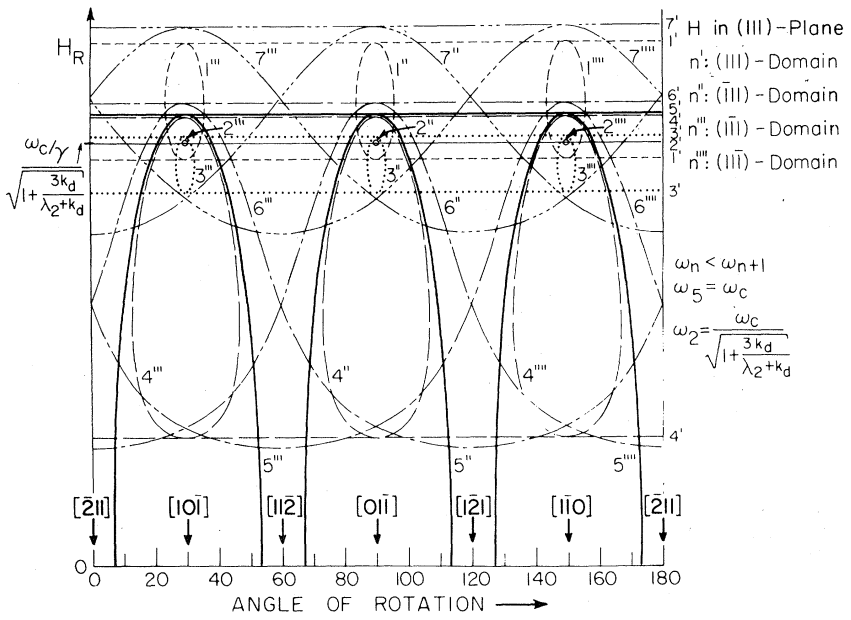

FIG. 4. Multidomain structure and anisotropy of the resonant field of an fcc type-II antiferromagnet with dipolar anisotropy, for the magnetic field lying in a (111) plane.

The special case, $\vec{h} \perp \vec{z}$, can be satisfied by rotating $\vec{h}$ in a general crystallographic plane. Sample orientation is not critical as there always exists an angle for which $\vec{h}$ is an EP. This angle is determined experimentally by the position at which ω^+ is extremal. The measurement of ω vs H at this angle provides a precise determination of $\kappa_d/(\lambda_2+\kappa_d)$. The special case $\vec{h} \| \vec{z}$ (a hard axis) is best studied experimentally with $\vec{h}$ in a (011) plane. Field rotations in this plane will bring $\vec{h}$ into alignment with the hard axes of the $[11\bar{1}]$ and $[1\bar{1}1]$ domains at which angles X^+ will be extremal. Small sample misalignment will have a second-order effect on X^+ making this plane ideal for the determination of X_c in the resonance equation and thus κ_d.

C. Extension to finite temperatures

In zero field, a finite temperature, $T < T_N$, produces a decrease in the sublattice magnetization. Using the mean-field approximation (MFA) and neglecting anisotropy one obtains[13]

$$M_1 = (g\mu_B S)\tfrac{1}{2} N B_S\left(\frac{g\mu_B S H_1^m}{kT}\right) ,$$

where H_1^m is the mean field acting on sublattice 1 and is given by

$$H_1^m = -\lambda_2 M_2 .$$

Symmetric relations hold for sublattice 2. An external field adds to the individual mean fields. For an easy plane, AFM in the spin-flopped state, and $h < h_E$, a geometrical calculation[14] shows that a changing applied field causes sublattice rotation (canting) with no length change, i.e., $|\vec{M}_1|$ independent of $\vec{H}$. The special form of the dipolar interaction leaves this result unchanged. Uniaxial or the full cubic magnetocrystalline anisotropy energy terms produce a field dependence of both direction and magnitude. For $h > h_E$ the sublattice magnetization will exhibit a "Brillouin functionlike" approach to saturation. The smallness of the in-plane anisotropy energy[5,7] and the cubic anisotropy constants K_1 and K_2 in related ferromagnetic europium chalcogenides[15] justifies their being neglected in what follows.

We represent the sublattice magnetization in the spin-flopped state ($h < h_E$) by

$$M_l(T) = a(T) M_0 , \tag{22}$$

where $a(0) = 1$. Replacing M_0 by $a(T)M_0$ in the definitions of $\vec{m}$, $\vec{l}$, and $\vec{h}$ gives the relations

$$\vec{m}^2 + \vec{l}^2 = a^2(T), \quad \vec{m}\cdot\vec{l} = 0 , \tag{23}$$

replacing Eq. (7), and the static equilibrium solutions

$$\vec{m} = \frac{\vec{h}_0}{\lambda_2+\kappa_d}; \quad \vec{l} = \left[a^2(T) - \left(\frac{h_0}{\lambda_2+\kappa_d}\right)^2\right]^{1/2} \hat{e}_y , \tag{24}$$

replacing Eqs. (9) and (10). (κ_a has been neglected in these and the following expressions for consistency with the approximation used.) The temperature-dependent exchange field and zero-field resonant fre-

quency are

$$h_E(T) = (\lambda_2 + \kappa_d) a(T) \tag{25a}$$

and

$$X_c^2(T) = 3\kappa_d(\lambda_2 + \kappa_d) a^2(T) \ . \tag{25b}$$

The general temperature-dependent resonant frequencies X^+ and X^- are obtained by substituting $l_{0y}(T)$ and $X_c(T)$ for l_{0y} and X_c in Eq. (15).

In the above, admittedly oversimplified, introduction of finite temperatures all quantities scale as the sublattice magnetization. This results in X_c and H_E having the same temperature dependence. Spin-wave and Green's-function analyses for the "easy-axis" Heisenberg AFM have been performed but are not directly applicable to EuTe, an easy-plane system. These results are discussed in Sec. V. Anticipating our experimental results we note that the critical frequency exhibits the *same* $T^{3/2}$ decrease with increasing temperature obtained for H_E in EuTe.

III. EXPERIMENTAL DETAILS

The compound EuTe was prepared by direct reaction of the elements and purified by fractional distillation in a high-temperature vacuum furnace. Single crystals are grown by evaporation and condensation of the material in the temperature gradient of a sealed tungsten crucible. Crystals were ground into spheres of 0.2- to 0.3-mm diameters, polished, and annealed at temperatures up to 950 °C. They were x-ray oriented and mounted such that the static magnetic field would lie in a (011) plane.

The basic microwave spectrometer operating from 60–90 GHz was assembled from standard microwave components. The klystrons used were cooled by a temperature controlled recirculating water bath for improved stability. Two different resonant-cavity–sample-holder assembly designs were employed for the cryogenic part of the spectrometer. Both employed double vacuum can construction and standard electronics for thermal isolation and control of the sample temperature.

The first assembly employed a continuously tunable Fabry-Perot cavity used as a reflection spectrometer and was used in the initial phase of this work. The cavity consists of a flat and a hemispherical focusing end-plate pair with an overall diameter large compared to the wavelengths used. Vacuum evaporation of gold onto these reflecting surfaces produced high Q response. The coupling iris and sample are placed at the centers of the flat and hemispherical end plates, respectively. The cavity is continuously tunable *in situ* at the operating temperature. Limitations of this cavity design originate in departures from ideal cylindrical symmetry and are manifest as a mode splitting associated with the two orthogonal polarizations. Tuning of the cavity is accompanied by rotation of the the hemispherical mirror and leads to an indeterminancy in the polarization as the frequency is changed. Used with a conventional electromagnet the static and microwave magnetic fields both lie in the (011) plane. Sensitivity to polarization required frequency selection for optimum signal strength. [Eqs. (A4a) and (A6a) illustrate the polarization dependence of the induced moments $\vec{m}_1$.] "Long line" or standing-wave effects associated with multiple reflections in a reflection spectrometer operating at cryogenic temperatures were a nuisance.

The above limitations have been eliminated by the following design: A transmission cavity was chosen having a rectangular cross section. The rectangular design provides control of the microwave polarization. The transmission feature, together with a good ferrite isolator minimizes the deleterious effect of standing waves in a long transmission line. (In transmission, standing waves can interfere with *the signal*, the frequency of maximum transmission, but have a minimal effect.) While this design is not continuously tunable, making the cavity very long produces a system with multiple resonance frequencies which are spaced sufficiently close for this work. The decreased filling factor was not a problem in the strongly absorbing magnetic material under study.

The transmission cavity has a symmetrical "U" shape in the H plane of the TE_{10} mode and is shown in Fig. 5. The cavity is fabricated from two copper blocks (inner and outer) and press fit together. The dot-dash line in Fig. 5 represents the boundary between the two sections. The cross section shown is the wave-guide broadwall with the boundary at the center line. The absence of transverse wall currents at the boundary between the two cavity halves contributes to the high Q's realized. The sample, inserted through a sidewall hole at the midpoint between the coupling irises, is situated at the lowest point of the "U". Sample rotation is in the plane of the electromagnet used. Rotation is effected by the shaft shown extending to the top of the sample holder. This direct rotation provision eliminates the need for gears at cryogenic temperatures and makes precise and continuous sample rotations relatively simple.

The cavity, though not tunable, has a length approximately equal to 80 half wavelengths at 85 GHz. Resonance frequencies occur at approximately 1.5 GHz intervals for both the odd and even half wavelength modes over the entire frequency range. Control of the microwave polarization is effected by selection of an odd or even frequency together with sample location in the cavity. The insets, Fig. 5, show the magnetic field lines in the cavity for the two modes. Using the odd mode with the sample near the cavity wall allows selection of parallel or perpendicular polarization in the plane of rotation by rotating the electromagnet. The third orthogonal polariza-

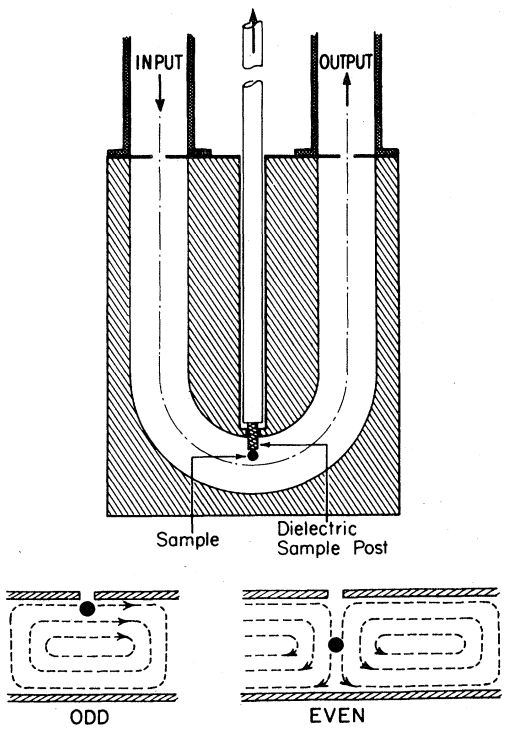

FIG. 5. Schematic drawing of transmission cavity employed. Coupling irises are shown by solid heavy lines just below the input and output arrows. The wave-guide cross section shown represents the rectangular wave-guide broadwall. The cavity is machined from two solid copper pieces press fit together along the dot-dash center line of the broadwall. The absence of transverse surface currents along this center line contributes to the high cavity Q. The insets represent the magnetic field lines and sample positioning for polarization control and are discussed in the text.

tion is realized by using an even mode and locating the sample at the cavity midpoint as shown. The basic cavity design is compatible with in *in situ* application of uniaxial stress along the axis of rotation but has not been so employed.

The ability to continuously rotate the sample with precision has led to an entirely new measuring method which has proven to be very useful for EuTe. This feature is most useful at the relatively high field, near the mode crossing. We write the resonance equation for the i th domain and a given plane of rotation in the form:

$$f_i(\omega, H, \phi) = 0 \ ,$$

where ω is the frequency, H is the magnetic field, and ϕ is the angle of rotation in the plane. The resonance behavior can in principle be studied by holding any two of the three parameters constant and varying the third. The larger the quantity, $(\partial f_i/\partial x)_{f_i=0}$, the easier becomes the observation of the resonance in sweeping x. It also leads to a smaller apparent linewidth. We note that near the gap frequency, ω_c, both $\partial f_i/\partial H$ and $\partial f_i/\partial \phi$ go asymptotically to zero as $\omega \to \omega_c$. Since continuous frequency variation at constant field and angle has not been available for this work, the gap frequency is determined by extrapolation from measurement at finite fields.

The multidomain resonance behavior has been investigated showing that at fixed frequencies $\omega \neq \omega_c$, the resonance equations are extremely sensitive to the rotation angle in a large range of fields. This is particularly true for $\omega < \omega_c$. In these regions of large angular sensitivity it is preferable to vary the *angle* and hold the field constant. It is emphasized that the two techniques—varying the angle at constant field and varying the field at constant angle—are complementary. The curves $(3', 3'', 3''')$ and $(4', 4'', 4''')$ for $\omega < \omega_c$ in Fig. 3 represent examples for which both methods must be used to optimally determine the complete resonance response. Examples are given in Sec. IV.

IV. EXPERIMENTAL RESULTS

The experimentally determined angular dependence of the resonance field at several different frequencies for $\vec{H}$ in a (011) plane is shown in Figs. 6–8. The solid curves represent the theoretical angular dependence calculated using Eq. (15) and values of ω_c and $3\kappa_d/(\lambda_2 + \kappa_d)$ chosen to best fit the data. The results in Figs. 6 and 7 correspond to the branch $X^+(\omega > \omega_c)$ and are to be compared with curves $(6', 6'', 6''')$ in Fig. 3. Figure 8 shows data obtained with $\omega < \omega_c$. The results shown in Fig. 6 were obtained with the Fabry-Perot cavity sweeping field at fixed angles. Two of the three resonances branches are observed. This indicates that the $(1\bar{1}1)$ domain and possibly the (111) domain were not present in this sample. Heat-

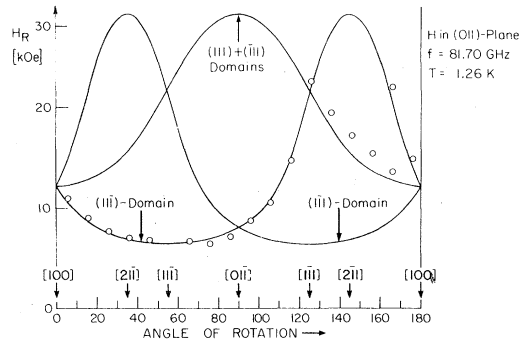

FIG. 6. Magnetic field for AFMR H_R of EuTe as a function of crystallographic orientation at the frequency 81.70 GHZ, with the magnetic field lying in a (011) plane. The solid curves are calculated by using the values ω_c and $3k_d(\lambda_2 + k_d)$ obtained from the fit in Fig. 9.

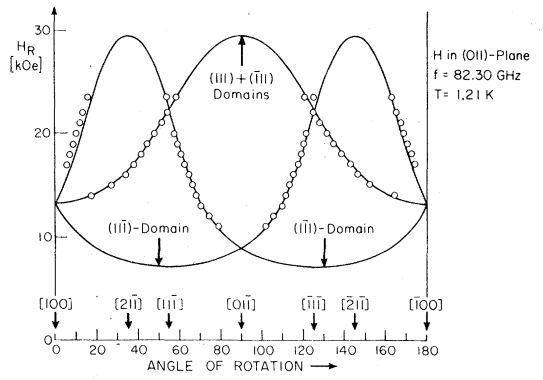

FIG. 7. Angular dependence of the resonant field at a frequency greater than ω_c. These results, obtained by angular rotation at fixed field, show contributions from each of the expected domain types.

ing to above Néel temperature, cooling to 1.26 K, and repeating the measurement reproduced these results. Experiments on other samples with the Fabry-Perot cavity sometimes exhibit resonance from a single domain.

The data shown in Fig. 7 were obtained with the transmission cavity. The magnetic field was held fixed and the angle varied to determine the resonance condition. In contrast to Fig. 6, all three branches corresponding to the four different T domains are observed and have comparable intensities. The fit of the measured singular dependence to the theoretical curves is very good. A deviation for the $(1\bar{1}1)$ domain in the interval 0–20° and to a lesser extent for the $(11\bar{1})$ domain in the interval 160–180° is noted. The observation of the four T domains in the transmission cavity and only one or two with the Fabry-Perot is not completely understood. We consider it probable that sample mounting with the Fabry-Perot cavity was *less* strain free with strain present while cooling through T_N causing one domain type to be dominant. The sensitivity of the absorption to microwave polarization is shown in the Appendix, Eqs. (A4a) and (A6a). The lack of polarization control with the Fabry-Perot cavity makes it possible that the domains were present but not observed due to an unfavorable polarization. We consider preferential domain formation in the presence of strain to be more probable.

The data shown in Figs. 6 and 7 were sensitive to microwave power level. Increasing power causes a line broadening and shift in the apparent resonant field. This effect became more pronounced at lower fields. For the applied field in the "easy plane" increasing power shifts the resonance to lower fields but when along a hard axis, the shift is to higher fields. A small temperature increase leading to a decrease in X_c would account for these shifts. Nonlinear response may also be important but has not been investigated. All results shown were obtained at power levels low enough to minimize these effects. Independent experiments with the sample immersed in superfluid helium reproduced satisfactorily those results at low powers in the helium exchange gas of our sample holders.

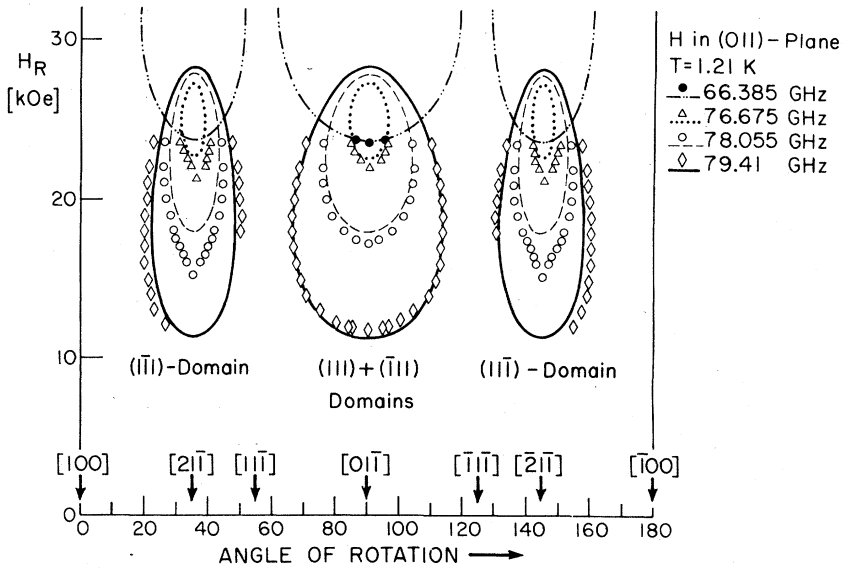

FIG. 8. Angular dependence of the resonant field at different fixed frequencies at and below the zero-field gap frequency $\omega_c \simeq 80$ GHz. Resonance contributions from the different domains are observed. The solid curves are the theoretical dependence.

Measurements at several frequencies for $\omega < \omega_c$ are shown in Fig. 8 obtained with the transmission cavity. Both the sweeping-angle and sweeping-field method were used to obtain these results. The absence of data above 24 kOe represents the field limit of the electromagnet used. As in Fig. 7 with $\omega > \omega_c$, the four different T domains are observed. The calculated angular dependence is in good agreement with the data but with signficant deviations for the nondegenerate $(1\bar{1}1)$ and $(11\bar{1})$ domains. Accompanying the resonance of the degenerate (111) and $(\bar{1}11)$ domains is a weak but well resolved satellite not shown in the figure. Its angular dependence is similar to that of the primary resonance but behaves as though representing a slightly lower gap frequency, ω_c. We tentatively assign the satellite to resonance in the domain-wall region between degenerate (111) and $(\bar{1}11)$ domains.

The resonance data at 66.385 GHz (solid circles in Fig. 8) correspond to the lower-frequency resonance branch. The $[01\bar{1}]$ direction corresponds to $\vec{H}$ in the easy plane of the degenerate (111) and $(\bar{1}11)$ domains. The polarization dependence of the absorption intensity has been determined. For the lower branch, X^-, maximum absorption occurs when the static and microwave fields are orthogonal. The upper branch, X^+, exhibits maximum absorption when the static and microwave fields are colinear. These results are in agreement with the calculated susceptibility tensor $\vec{\vec{\chi}}(m)$, Eq. (A4a).

The dependence of resonance frequency on field at two different temperatures with $\vec{H}$ along a hard axis and in the "easy plane" is shown in Fig. 9. These data, obtained with the Fabry-Perot cavity, were reported in Ref. 10. The resonant frequency-field relation, Eq. (A3a), for $\vec{H}$ in the easy plane is

$$X^{+2} = X_c^2 l_{0y}^2$$

or

$$\left(\frac{\omega^+}{2\gamma M_0}\right)^2 = (\lambda_2 + \kappa_d)(3\kappa_d + \kappa_a) \times \left[1 - \frac{1}{(\lambda_2 + \kappa_d)^2}\left(\frac{H_0}{2M_0}\right)^2\right] .$$

Plotting $(\omega^+)^2$ vs H^2 and extrapolating to $H = 0$ provides a determination of the zero-field frequency, X_c. The slope gives the exchange field, h_E^0.[12]

The temperature dependence of X_c determined with the transmission cavity is shown in Fig. 10. The variation is in good agreement with earlier results[10] obtained using a different sample and the Fabry-Perot cavity. Plotting the results versus $T^{3/2}$ gives a good fit for $T \leq 3$ K and extrapolates to $\nu_c^0 = 80.87 \pm 0.2$ GHz at $T = 0$. Alternatively, the data for $T \leq 6$ K is better fit by a T^2 dependence extrapolating to $\nu_c^0 = 80.65 \pm 0.2$ GHZ at $T = 0$.

The exchange field, H_E, has been determined from the slope of $(\omega^+)^2$ vs H_0^2 in applied fields $H < 24$ kOe. The uncertainty in the values determined increases rapidly with increasing temperature. The limited precision available precludes a meaningful determination of the dependence of H_E on T. We have assumed that H_E scales with T in the same way as ω_c obtaining $H_E = 76.7$ kOe at $T = 0$.

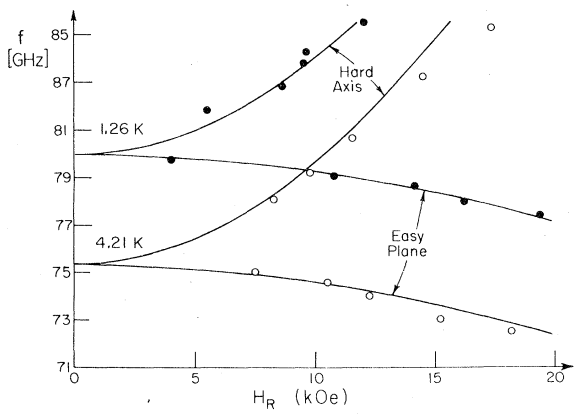

FIG. 9. Resonance frequency vs field for the directions $\vec{H} \| \vec{z}$ [Hard axis: Eq. (A5a)] and $\vec{H} \| \vec{x}$ [Easy plane: Eq. (A3a)] at two temperatures. The solid curves represent the results of fitting to these equations.

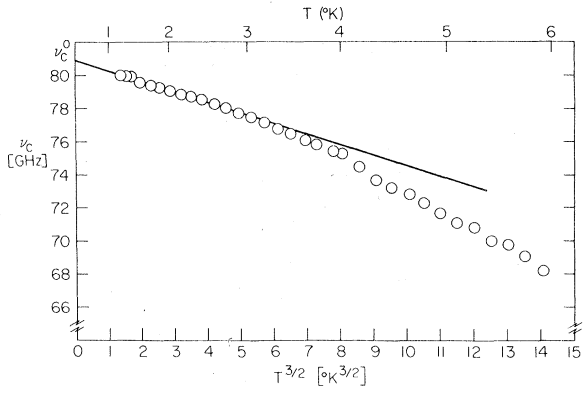

FIG. 10. Temperature dependence of the zero-field resonance frequency, $\nu_c(T)$. Individual points have been obtained by fitting the frequency vs field dependence with H in an easy plane as shown in Fig. 9. The solid curve drawn through the points with $T \lesssim 3$ K is the limiting $T^{3/2}$ dependence. The limiting value at $T = 0$ is $\nu_c^0 = 80.87 \pm 0.2$ GHz.

V. DISCUSSION AND CONCLUSIONS

Previous AFMR results in EuTe[1,5,7] have shown that it is an easy plane AFM and have been interpreted in terms of the dipolar and a phenomenological in-plane anisotropy energy. The zero-field resonance frequencies[5]

$$\omega_c^- = 2 \text{ GHz and } \omega_c^+ = 68 \text{ GHz}$$

were determined by fitting the angular dependences of the low-frequency branch. The frequency ω_c^+ (X_c in the notation of this paper) determined corresponds to a dipolar anisotropy energy ~20% *lower* than the classically calculated value.

We have measured the high-frequency AFMR In EuTe at different frequencies and directions of $\vec{H}$ in a (011) plane. The angular dependence of the resonance field at fixed frequencies both greater and less than ω_c have been analyzed in terms of the dipolar and a phenomenological uniaxial anisotropy energy. Resonance branches associated with the different T domains are observed. Fitting the measured angular dependences using κ_d and λ_2 with $\kappa_a = 0$ gives very good agreement with the theoretical expressions.

The resonance frequency versus field has been determined for $\vec{H}$ parallel and perpendicular to an easy plane at different temperatures. The values of ν_c and H_E were determined as a function of temperature. Extrapolation to $T = 0$ gives

$$\nu_c(0) = 80.87 \text{ GHz}, \quad H_E(0) = 76.7 \text{ kOe} .$$

In Sec. II it was noted that the demagnetizing energy is not negligible compared to the exchange and dipolar anisotropy energies in EuTe. Applying the demagnetization correction for a spherical sample gives the values

$$\bar{\nu}_c(0) = 78.91 \pm 0.2 \text{ GHz}, \quad \bar{H}_E(0) = 73.0 \text{ kOe}.$$

Oliveira *et al.*[16] have determined $H_E(T)$ directly from measurements of M vs H at the high-field boundary between the canted and paramagnetic phases. Their result at $T = 0$, $H_c(0) = 72.2 \pm 0.1$ kOe, also expressed as an internal field, is in very good agreement with our value. It must be remarked that the good agreement with Oliveira *et al.*[16] is partially fortuitous. As the canted-paramagnetic phase boundary is approached ($H \leq H_E$) the variation in M is greater than linear in H. Jacobs and Silverstein[17] have interpreted this nonlinear variation in terms of zero-point spin-wave contributions to the free energy. The critical field will be lower than the mean-field result. Our results, obtained in fields less than 24 kOe, are based on measurements far from the critical field. It is surprising that this parameter determined at and far from the region in which critical fluctuations and/or zero-point spin-wave contributions are important should agree so well.

The dipolar interaction constant at $T = 0$, $K_d = \kappa_d M_0^2$, has been determined from the experimental values of $\nu_c(0)$ and $H_E(0)$. The result

$$K_d = (0.817 \pm 0.015) \times 10^6 \text{ ergs/cm}^3$$

is to be compared with the value calculated classically[6] for EuTe, $K_d^{\text{th}} = 0.732 \times 10^6$ ergs/cm^3. The experimental value is ~10% *greater* than the theoretical result. This difference would be explained by a uniaxial anisotropy term, κ_a, induced by the lattice distortion which normally accompanies AFM ordering. Estimates based on the anisotropy constants in EuO and EuS[15] indicate that single-ion magnetocrystalline anisotropy constants are too small to account for this discrepancy.[15] A second explanation could be the neglect of quantum-mechanical corrections to the dipolar energy.

Oliveira *et al.*[16] have measured the temperature dependence of the critical field, $H_c(T)$. They find that $H_c(T)$ decreases at $T^{3/2}$ in the interval $1 \lesssim T \lesssim 4$ K. Anderson and Callen[18] have applied a Green's-function analysis to the canted-paramagnetic phase boundary finding a leading $T^{3/2}$ dependence for $H_c(T)$ arising from the renormalization of the spin-wave energies. Feder and Pytte[19] have obtained a similar result for a uniaxial Heisenberg AFM using spin-wave theory including spin-wave interactions to leading order in $1/2S$. The $T^{3/2}$ decrease in the zero-field resonance frequency, Fig. 10, suggests spin-wave renormalization of the resonance frequency. We note that in both Refs. 18 and 19 the model considered is an easy-axis AFM in contrast to the easy-plane behavior of EuTe and is not directly applicable to this material.

The presence of multiple T domains in EuTe and the strain associated with domain-wall boundaries has been observed as a small satellite absorption. The presence of strain is also, most likely, the origin of the deviations observed in Fig. 8 and can be expected to contribute a broadening to the resonance lines. We have attempted to influence the domain structure by cooling through T_N in magnetic fields up to 24 kOe without notable results. Alternatively, cooling through T_N with uniaxial stress along a [111] direction followed by its removal at $T < T_N$ could likely produce single-domain samples. Careful measurement of the field-frequency dependence in single-domain sample with $\vec{H}$ in the corresponding (111), easy plane as a function of temperature could provide a measurement of $\nu_c(T)$ and $H_E(T)$. A determination of $H_E(T)$ in the field region far from $H_c(T)$ would provide an experimental method of determining the explicit effect of critical fluctuations.

ACKNOWLEDGMENT

The principal parts of this work were completed under the ERDA (DOE) Contract No. E(04-3)-34.P.A.77.

APPENDIX

The susceptibility tensors, $\vec{\vec{\chi}}(m)$ and $\vec{\vec{\chi}}(l)$, have been calculated for general field directions in the x-z plane. The absorptive part of the susceptibility is introduced using the Plemelj formula

$$\lim_{\eta\to 0}\left(\frac{1}{X-\bar{X}+i\eta}\right)=P\left(\frac{1}{X-\bar{X}}\right)-i\pi\delta(X-\bar{X}) \quad . \tag{A1}$$

The determinant Δ, Eq. (14), is expanded as

$$-\frac{1}{\Delta}=\frac{1}{2X^2}\frac{1}{(X^{+2}-X^{-2}}\left[\frac{1}{X^+}\left(\frac{1}{(X-X^+)}-\frac{1}{(X+X^+)}\right)-\frac{1}{X^-}\left(\frac{1}{(X-X^-)}-\frac{1}{(X+X^-)}\right)\right] \quad . \tag{A2}$$

Introducing the function

$$R^{\pm}(x)=\frac{1}{X^{+2}-X^{-2}}\left(-\frac{1}{(X^2-X^{\pm 2})}+\frac{i\pi}{2X^{\pm}}[\delta(X-X^{\pm})-\delta(X+X^{\pm})]\right)$$

the susceptibility components $\chi_{ij}(m)$ are given below. The frequencies, X^+ and X^-, are given by Eq. (15).

$$\chi_{xx}(m)=(\lambda_2+\kappa_d+\kappa_a)X_c^2 l_{0y}^2 m_{0x}^2[R^-(X)-R^+(X)]+[(3\kappa_d+\kappa_a)l_{0y}^2+(\lambda_2+\kappa_d)m_{0z}^2][X^{+2}R^+(X)-X^{-2}R^-(X)] \quad ,$$

$$\chi_{yy}(m)=(\lambda_2+\kappa_d+\kappa_a)X_c^2 l_{0y}^2 m_{0x}^2[R^-(X)-R^+(X)]$$
$$+[(\lambda_2+\kappa_d+\kappa_a)m_{0x}^2+(\lambda_2+\kappa_d)m_{0z}^2][X^{+2}R^+(X)-X^{-2}R^-(X)] \quad ,$$

$$\chi_{zz}(m)=(\lambda_2+\kappa_d)m_{0x}^2[(X_c^2 l_{0y}^2-X^{-2})R^-(X)-(X_c^2 l_{0y}^2-X^{+2})R^+(X)] \quad ,$$

$$\chi_{xy}(m)=-\chi_{yx}(m)=(ix)m_{0z}[X^{+2}R^+(X)-X^{-2}R^-(X)] \quad ,$$

$$\chi_{xz}(m)=-\chi_{zx}(m)=(\lambda_2+\kappa_d)m_{0x}m_{0z}[X^{-2}R^-(X)-X^{+2}R^+(X)] \quad ,$$

$$\chi_{yz}(m)=-\chi_{zy}(m)=(ix)m_{0x}[(X_c^2 l_{0y}^2-X^{-2})R^-(X)-(X_c^2 l_{0y}^2-X^{+2})R^+(X)] \quad .$$

The susceptibility components $\chi_{ij}(l)$ are

$$\chi_{xx}(l)=(\lambda_2+\kappa_d)(\lambda_2+\kappa_d+\kappa_a)(ix)l_{0y}m_{0x}m_{0z}[R^+(X)-R^-(X)] \quad ,$$

$$\chi_{yy}(l)=X_c^2(ix)m_{0x}m_{0z}[R^-(X)-R^+(X)] \quad ,$$

$$\chi_{zz}(l)=(\lambda_2+\kappa_d)^2(ix)l_{0y}m_{0x}m_{0z}[R^-(X)-R^+(X)] \quad ,$$

$$\chi_{xy}(l)=(\lambda_2+\kappa_d+\kappa_a)l_{0y}m_{0x}[(X_c^2 l_{0y}^2-X^{+2})R^+(X)-(X_c^2 l_{0y}^2-X^{-2})R^-(X)] \quad ,$$

$$\chi_{yx}(l)=(\lambda_2+\kappa_d+\kappa_a)X_c^2 l_{0y}^2 m_{0x}^2[R^+(X)-R^-(X)]+(3\kappa_d+\kappa_a)l_{0y}m_{0x}[X^{-2}R^-(X)-X^{+2}R^+(X)] \quad ,$$

$$\chi_{xz}(l)=(ix)l_{0y}[X_c^2 l_{0y}^2+(\lambda_2+\kappa_d)^2 m_{0z}^2][R^+(X)-R^-(X)]+(ix)l_{0y}[X^{-2}R^-(X)-X^{+2}R^+(X)] \quad ,$$

$$\chi_{zx}(l)=(\lambda_2+\kappa_d)(\lambda_2+\kappa_d+\kappa_a)(ix)l_{0y}m_{0x}^2[R^-(X)-R^+(X)]$$
$$+(ix)l_{0y}[X^{+2}R^+(X)-X^{-2}R^-(X)] \quad ,$$

$$\chi_{yz}(l)=(\lambda_2+\kappa_d)X_c^2 l_{0y}m_{0x}^2 m_{0z}[R^+(X)-R^-(X)] \quad ,$$

$$\chi_{zy}(l)=(\lambda_2+\kappa_d)l_{0y}m_{0z}[X^{-2}R^-(X)-X^{+2}R^+(X)] \quad .$$

The form of these tensors is illustrated below for $\vec{h}$ parallel and perpendicular to the easy plane.

A. $\vec{h} \| \vec{x}$: Easy plane

For $\vec{h}$ in the EP, $h_z = 0$, the frequencies are

$$X^{+2} = X_c^2 l_{0y}^2 \ , \tag{A3a}$$

$$X^{-2} = (\lambda_2 + \kappa_d)(\lambda_2 + \kappa_d + \kappa_a) m_{0x}^2 \ , \tag{A3b}$$

with

$$\vec{\vec{\chi}}(m) = \begin{pmatrix} \dfrac{-(3\kappa_d + \kappa_a) l_{0y}^2}{X^2 - X^{+2}} & 0 & 0 \\ 0 & -\dfrac{(\lambda_2 + \kappa_d + \kappa_a) m_{0x}^2}{X^2 - X^{-2}} & -\dfrac{(ix) m_{0x}}{X^2 - X^{-2}} \\ 0 & \dfrac{(ix) m_{0x}}{X^2 - X^{-2}} & \dfrac{(\lambda_2 + \kappa_d) m_{0x}^2}{X^2 - X^{-2}} \end{pmatrix} . \tag{A4a}$$

and

$$\vec{\vec{\chi}}(l) = \begin{pmatrix} 0 & \dfrac{(\lambda_2 + \kappa_d + \kappa_a) l_{0y} m_{0x}}{X^2 - X^{-2}} & \dfrac{(ix) l_{0y}}{X^2 - X^{-2}} \\ \dfrac{(3\kappa_d + \kappa_a) l_{0y} m_{0x}}{X^2 - X^{+2}} & 0 & 0 \\ \dfrac{-(ix) l_{0y}}{X^2 - X^{+2}} & 0 & 0 \end{pmatrix} . \tag{A4b}$$

B. $\vec{h} \| z$: Hard axis

For $\vec{h}$ perpendicular to the EP, the frequencies are

$$X^{+2} = X_c^2 l_{0y}^2 + (\lambda_2 + \kappa_d) m_{0z}^2 \ , \tag{A5A}$$

$$X^{-2} = 0 \ , \tag{A5b}$$

with

$$\vec{\vec{\chi}}(m) = \begin{pmatrix} -\dfrac{1}{(\lambda_2 + \kappa_d)} \dfrac{X^{+2}}{X^2 - X^{+2}} & -\dfrac{(ix) m_{0z}}{X^2 - X^{+2}} & 0 \\ \dfrac{(ix) m_{0z}}{X^2 - X^{+2}} & -\dfrac{(\lambda_2 + \kappa_d) m_{0z}^2}{X^2 - X^{+2}} & 0 \\ 0 & 0 & 0 \end{pmatrix} \tag{A6a}$$

and

$$\vec{\vec{\chi}}(l) = \begin{pmatrix} 0 & 0 & -\dfrac{l_{0y}}{jx} \\ 0 & 0 & 0 \\ \dfrac{-(ix) l_{0y}}{X^2 - X^{+2}} & \dfrac{(\lambda_2 + \kappa_d) l_{0y} m_{0z}}{X^2 - X^{+2}} & 0 \end{pmatrix} . \tag{A6b}$$

---

*Present address: Brown, Boveri, and Cie., AG, CH-5401 Baden, Switzerland.

[1]J. W. Battles and G. E. Everett, Solid State Commun. 6, 569 (1968).

[2]E. A. Turov, *Physical Properties of Magnetically Ordered Crystals* (Academic, New York, 1965), Chap. IV.

[3]Antiferromagnetic vector $\vec{l}$ is also referred to as the staggered magnetization.

[4]Constants are

$$H_E = (A + a)/M_0, \quad H_A = |b|/M_0, \quad H_{EA} = (H_E H_A)^{1/2} \ .$$

[5]J. W. Battles and G. E. Everett, Phys. Rev. B 1, 3021 (1970).

[6]J. I. Kaplan, J. Chem. Phys. 22, 1709 (1954).

[7]Jun NaKai, Satoru Kunii, and Eiji Hirahara, J. Phys. Soc. Jpn. 34, 917 (1973).

[8]F. Masset and J. Callaway, Phys. Rev. B 2, 3657 (1970).
[9]B. Passenheim, Ph.D. thesis (University of California, Riverside, 1969) (unpublished).
[10]G.E. Everett and P. Streit, in *Proceedings of the International Magnetism Conference, Moscow, 1973* (Nauka, Moscow, 1974), Vol. 4, p. 136.
[11]In Eq. (2), M_0 represented the total moment at paramagnetic saturation.
[12]Exchange field is determined by the condition $\vec{l}=0$ and is anisotropic. For $\vec{h}$ in the x-z plane at an angle β with respect to the z axis the exchange field is given by

$$h_E(\beta)=\frac{h_E^0+\kappa_a}{\left[1+\frac{2\kappa_a}{H_E^0}\left(1+\frac{\kappa_a}{2h_E^0}\right)\sin^2\beta\right]^{1/2}},$$

where $h_E^0=\lambda_2+\kappa_a$.
[13]B. Lax and K. Button, *Microwave Ferrites and Ferrimagnetics* (McGraw-Hill, New York, 1962).
[14]C. Garrett, J. Chem. Phys. 19, 1154 (1951).
[15]N. Miyata and B. E. Argyle, Phys. Rev. 157, 448 (1967); G. E. Everett and R. A. Ketcham, J. Phys. (Paris) 32, C1-545 (1971); and Richard S. Hughes, Glen E. Everett, and A. W. Lawson, Phys. Rev. B 9, 2394 (1974).
[16]N. F. Oliveira, Jr., S. Foner, Y. Shapira, and T. B. Reed, Phys. Rev. B 5, 2634 (1972).
[17]I. S. Jacobs and S. D. Silverstein, Phys. Rev. Lett. 13, 272 (1974).
[18]F. Burr Anderson and Herbert B. Callen, Phys. Rev. 136, A1068 (1964); also Harold Falk, Phys. Rev. 133, A1382 (1964).
[19]J. Feder and E. Pytte, Phys. Rev. 168, 640 (1968).